Research papers

Hydraulic head fluctuations in an intermediate depth coastal surface aquifer

Rachel Housego [a,b,*], Britt Raubenheimer [b,*], Steve Elgar [b], Ming Zhi Wu [c]

[a] *MIT-WHOI Joint Program in Oceanography, 86 Water St., Woods Hole, MA 02543, MS #12, USA*
[b] *Department of Applied Ocean Science and Engineering, Woods Hole Oceanographic Institution, 266 Woods Hole Rd., Woods Hole, MA 02543, USA*
[c] *Pells Sullivan Meynink, 22 Delhi Street, West Perth, WA 6005, Australia*

ABSTRACT

Tides and storm surges are important drivers of groundwater circulation and fluxes in coastal aquifers. However, few field studies have characterized the response of the coastal aquifer to both forcings. Here, three years of hydraulic head observations in a roughly 20-m deep barrier island surface aquifer are used to investigate the inland propagation of fluctuations driven by ocean water-level changes owing to diurnal and semi-diurnal tides and storm-induced surge and wave-driven setup. Similar to prior observations, the observed rate of amplitude attenuation of the hydraulic head fluctuations is higher than the inland increase in phase lag for the tidally-driven head fluctuations. Additionally, tidal hydraulic head fluctuations deeper in the aquifer lead those nearer the surface of the aquifer. In contrast, storm surges with periods of several days have similar rates of amplitude attenuation and inland increase in phase lags, and hydraulic head fluctuations are roughly depth uniform. A nonlinear, intermediate aquifer-depth theory (not previously compared with field observations) describes the inland and vertical changes of tidal amplitudes and phase lags, and collapses to the linear solution for long period fluctuations, consistent with the storm surge observations. The diffusivity estimated by fitting intermediate depth solutions to the observed tidal amplitude attenuation and rate of inland phase lag is consistent with the aquifer properties, providing a method to characterize aquifers using coastal head observations. Numerical model simulations neglecting capillary effects, hysteresis, and vertical layering (which can cause discrepancies between amplitude attenuation and phase lag evolution) are similar to the observations and support the importance of the depth of the aquifer relative to the wavelength of the hydraulic head fluctuations.

1. Introduction

Fluctuations in ocean water levels owing to tides and storms cause fluctuations in the hydraulic head at the surface aquifer-ocean interface, which generate waves that propagate inland (Anderson and Lauer, 2008; Cartwright et al., 2004; Cartwright and Gibbes, 2011; Erskine, 1991; Ferris, 1951; Jacob, 1950; Nielsen, 1990; Raubenheimer et al., 1999; Rotzoll and El-Kadi, 2008; Trglavcnik et al., 2018). The hydraulic gradients resulting from the groundwater waves influence mixing between ocean water and freshwater within the aquifer, affect the fate and transport of contaminants, and modulate the rate of groundwater discharge to the ocean (Boufadel et al., 2007; Moore, 2010; Robinson et al., 2006, 2014), and also may affect sediment transport and evolution of the beach profile (Bakhtyar et al., 2013; Chardón-Maldonado et al., 2016; Sous et al., 2013; Turner and Masselink 1998; Xin et al 2010).

Elevated groundwater levels also can cause groundwater flooding, mobilize pollutants, and affect beach stability (Befus et al., 2020; Grant et al., 2021; Rotzoll and Fletcher, 2013; Threndyle et al., 2022).

As hydraulic head waves propagate inland their amplitudes decrease (attenuate) and their arrival times increase (a phase lag equal to the distance traveled divided by the wave speed normalized by the wave period) relative to the ocean fluctuations. The propagation of hydraulic head fluctuations (including amplitude attenuation and speed or phase lag) depends on the period of the water-level oscillation, aquifer properties (e.g., hydraulic conductivity (K), specific yield (S_y), aquifer depth (z)), and aquifer configuration (e.g., heterogeneity, layering). Aquifer sediments act as a low-pass filter, and high-frequency oceanic fluctuations (individual wind-waves) are attenuated within a few meters inland from the beach face. Longer period (multi-day) changes in the ocean water level owing to storms (surge and wave-driven setup, Longuet-

---

Higgins and Stewart, 1964) penetrate farther into the aquifer than those driven by lunar or solar tides (Yu et al., 2022a,b). Hydraulic head fluctuations in aquifers with larger hydraulic diffusivities (a function of K, z, S_y) propagate father inland with less amplitude damping and phase shift than those in aquifers with smaller hydraulic diffusivities.

Analytical solutions describe the propagation of tidal (the Jacob-Ferris model, Ferris, 1951; Jacob, 1950) and storm-driven (Cartwright and Gibbes, 2011; Li et al., 2004; Rotzoll and El-Kadi, 2008) groundwater waves through homogeneous, isotropic, shallow coastal surface aquifers with vertical ocean boundaries. Forecasts of coastal flooding resulting from ocean-driven groundwater increases owing to sea level rise and storm intensification, which are important for coastal management, often are based on these linear theory solutions (Vitousek et al., 2017; Woodruff et al., 2013). However, amplitude decay rates estimated from observations can be 2 or 3 times larger than expected from linear theory in comparison with phase lag rates, resulting in uncertainty in the estimates of aquifer parameters (Erskine, 1991; Fakir and Razack, 2003; Nielsen, 1990; Rotzoll and El-Kadi, 2008; Smith and Hick, 2001; Trefry and Bekele, 2004). The ability of higher-order theories to characterize natural aquifers is unknown.

Non-shallow aquifers have been encountered in studies around the world, including Australia (Robinson et al., 2007; Trefry and Bekele 2004), Japan (Uchiyama et al., 2000), Germany (Röper et al., 2013), UK (Erskine, 1991), and the USA (Schultz and Ruppel, 2002). Despite several studies indicating the importance of aquifer depth (Parlange, 1984; Nielsen et al., 1997; Robinson et al., 2007), many studies of coastal water table fluctuations do not report all of the geologic information (depth, hydraulic conductivity, and specific yield) necessary to evaluate higher-order solutions and neglect the potential effects of aquifer depth (Carr and Van der Kamp 1969; Cartwright, 2004; Fadili et al., 2016; Fakir and Razack, 2003; Jha et al., 2008; Nielsen 1990; Robinson et al., 2006; Sous et al., 2016, and many more). Additionally, a wide range of ocean wave periods is needed to identify aquifer depth effects on the propagation of hydraulic head fluctuations, but few field studies have had long enough durations to examine hydraulic head fluctuations driven by both tides and storm surges. Consequently, the effect of aquifer depth on the propagation of water table fluctuations driven by tides and surges in field data is not known.

Analytical solutions have been developed to account for the effects of non-shallow (relative to a wavelength) aquifer depths (Nielsen et al., 1997). Although these higher-order (nonlinear) theories of propagation of groundwater fluctuations have been validated in laboratory experiments (Cartwright et al., 2004; Shoushtari et al., 2016), little data are available on propagation of groundwater fluctuations in field settings where multiple forcing frequencies (e.g., tides, surges) act simultaneously on the aquifer. Furthermore, the relative importance of the nonlinear terms is uncertain in heterogeneous field conditions. Accurate characterization of the dispersion of tide and storm signals in coastal aquifers is essential for predicting the water table elevation and hydraulic gradients near the coast.

Here, a novel three-year long data set of ocean water levels and hydraulic heads (Section 2) describes the response of the unconfined coastal surface aquifer to both tides (semi-diurnal and diurnal) and storm surges (n = 26). The hydraulic head measurements span the area from the dune crest to about 300 m inland and include vertical information at 5 different depths behind the dune. These measurements are used to evaluate linear and higher-order intermediate-depth theories (Section 3) for both the inland propagation and vertical structure of the hydraulic head response to storms and tides. Observed tidal amplitude attenuation rates are nearly twice those of phase lag rates (Section 4) and the hydraulic head fluctuations deeper in the aquifer lead those closer to the water table. Comparisons of the observations with analytical theories suggest that (nonlinear) intermediate-depth aquifer solutions represent the cross-shore and vertical structure of tidal head fluctuations in this approximately 20-m-deep aquifer, whereas linear shallow aquifer theory describes the longer period (and wavelength)

storm fluctuations. This is the first data set to show propagation of hydraulic head fluctuations consistent with higher-order (intermediate depth) analytical theories using environmental data. Numerical model simulations (MODFLOW-NWT) analyzed inland of the dune (Section 5) are consistent with the observed tidal propagation, supporting the theoretical assumptions. These simulations show that in some environments the propagation of hydraulic head fluctuations can be reproduced accurately without the additional complexity of variable-density and unsaturated zone processes. Methods for applying higher-order theories to characterize large-scale hydrogeological aquifer properties also are presented, including a discussion of the challenges and uncertainties, such as the effects of seasonal and storm-driven changes of inland heads and saline plumes (Section 6). These results have implications for aquifer characterization and predicting water table elevations in the coastal zone.

2. Field study

2.1. Site description

Observations were collected in Dare County, NC, near the village of Duck. The area is part of the North Carolina Outer Banks, which is a 320-km long chain of barrier islands extending south from the Virginia-North Carolina state line to Bogue Inlet and is part of the North Carolina Coastal Plain aquifer system. The shallow geology is a 50–70 m thick Quaternary sequence that fills the Albemarle Embayment (Lautier, 2009; Winner and Coble, 1996). The surficial aquifer typically is comprised of > 70% sand (Winner and Coble, 1996). A network of paleo-channels containing muddy estuarine sediment, sand, and fluvial gravel that were backfilled with younger Pleistocene sediments also weaves through the Quaternary sequence (Lazarus and Murray, 2011; Riggs et al., 1995). The surficial aquifer is underlain by clay and silt beds that comprise the Yorktown confining unit, which extends throughout the northern half of the NC Coastal Plain and attains a thickness of >100 m in Dare County (Mallinson et al., 2010; Winner and Coble, 1996). The area surrounding the observations is undeveloped, and during the observation period there was no local pumping from the aquifer.

In September 2014, 12 groundwater wells were installed at 4 locations along a transect on the ocean-side of the barrier island, extending from behind the dune to 160 m inland, at the U.S. Army Corps of Engineers Coastal Hydraulics Laboratory Field Research Facility (FRF, https://www.frf.usace.army.mil) in Duck, NC (Fig. 1, and Housego et al., 2021). An additional well was located near the center (highest point) of the island, at x ~ 300 m, and provided observations used to initialize the idealized numerical model. The property is bordered on the west by Currituck Sound and on the east by the Atlantic Ocean. On the ocean side of the island, the beach (slope ~ 0.1) is backed by ~ 7-m-high vegetated dunes. Over the observation period there was little change in the vegetation location and type. Sediment samples collected during construction of the facility (Meisburger et al., 1989) and during installation of the groundwater wells suggest that the surficial aquifer is composed of medium quartz sand (mean diameter ~ 0.25 mm) and shell hash. Prior studies suggest the uppermost confining layer is roughly 15 to 30 m below NAVD88 (approximately mean sea level) (Manahan et al., 1998; Meisburger et al., 1989). However, a confining unit was not encountered during drilling, with boreholes extending from 15 (under the dune) to 26 m (near the sound) below NAVD88. Prior estimates of the hydraulic conductivity K in the surface aquifer near this site range from about 15 to 90 m/d (Manahan et al, 1998; Turner and Masselink, 1998). Additionally, although paleochannels are present throughout the Outer Banks, a prior side-scan sonar survey of the Duck study site did not identify any distinct channels or gravel outcrops (Browder and McNinch, 2006). Based on these observations, the aquifer is assumed approximately uniform across the island at the FRF.
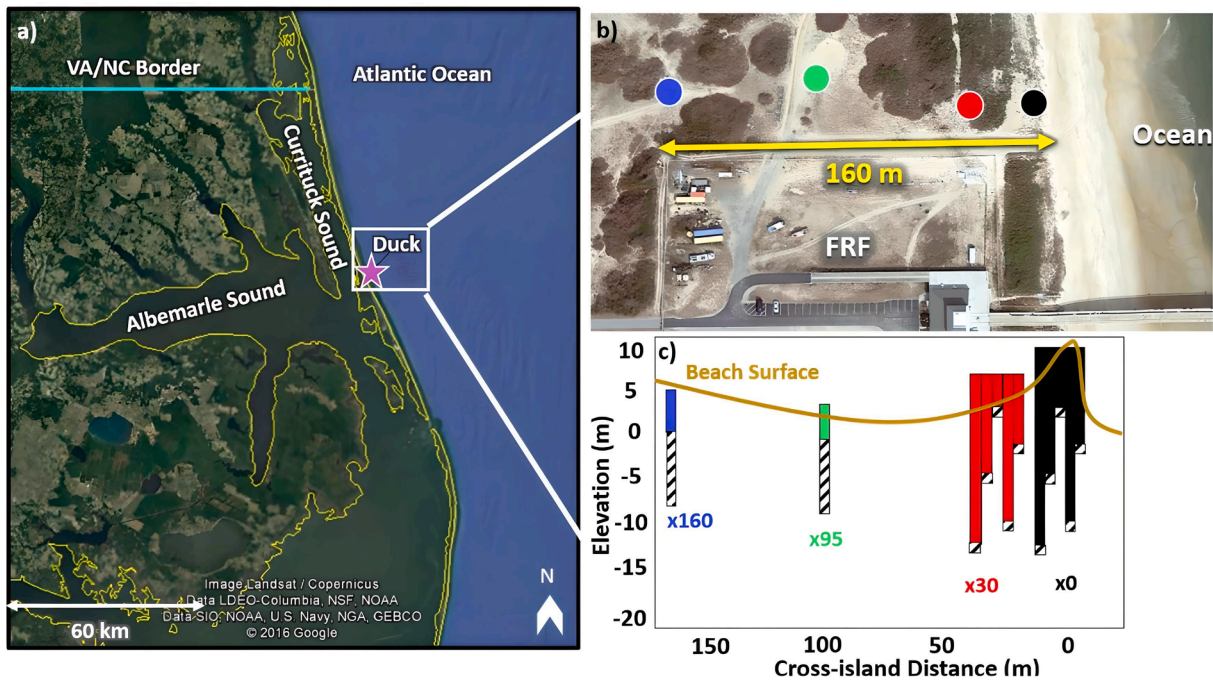
Fig. 1. a) Google Earth image of the North Carolina Outer Banks. The border of the land is outlined in yellow. The Duck, NC U.S. Army Corps of Engineers Field Research Facility (FRF) is indicated by the purple star and is located on a barrier island between Currituck Sound and the Atlantic Ocean. **b)** Aerial view of the 4 groundwater well locations (colored circles). **c)** Elevation of the beach surface (tan curve) and groundwater wells (colored rectangles) versus cross-island distance. Wells in clusters are separated 3 m in the alongshore (in-out of the page). The crosshatched region on each well is the screened section. The number below each well location is the distance (m) from the dune crest (black circle). (For interpretation of the references to color in this figure legend, the reader is referred to the web version of this article.)

2.2. Observations

The cross-shore positions (x, positive toward the sound) of the well locations are defined relative to the dune crest. Each well is composed of 0.05 m-diameter PVC pipe with No.10 perforated screen at the bottom surrounded by gravel pack topped with a bentonite seal. At the two locations nearest the ocean (Fig. 1b, red and black circles), well clusters (Fig. 1c) were installed to measure the vertical variation in the groundwater structure (Church and Granato, 1996; Elci et al., 2001; Levanon et al., 2013). Wells in the clusters had 0.6-m-long screens and were separated 3 m in the alongshore. Shallow and deep wells were staggered to minimize interference between wells. The clusters consisted of 5 wells installed to depths ranging from −0.5 to −15.4 m (NAVD88). Conductivity-temperature-depth (CTD) sensors at about mid-screen-elevation in each well were sampled at 10 min intervals. Water density is calculated (Fofonoff and Millard, 1983) from the measured salinity, temperature, and pressure. The sensors were vented to the atmosphere so that pressure measurements are not influenced by fluctuations in barometric pressure. Sensor elevations were estimated using differential GPS measurements of the well cap, and simultaneous water-level measurements (from a standard meter) and pressure and water density measurements from the in-situ sensors. Annual re-estimates show <0.02 m drift. Freshwater equivalent hydraulic heads h_f are estimated from the pressure measurements as,

$$h_f = \frac{p}{\rho_f g} + z_s \tag{1}$$

where p (Pa) is the measured pressure, ρ_f (kg/m^3) is the density of freshwater, g (m/s^2) is the gravitational constant, and z_s (m) is the elevation of the sensor (relative to NAVD88).

The ocean beach is surveyed monthly, and has an intertidal slope (β) of about 0.1. Ocean water levels measured every 6 min with a NOAA tide gauge (ID **8651371**) in about 8 m depth at the end of the FRF pier indicate the tides are primarily semi-diurnal with range ~ 1 m (Fig. 2),
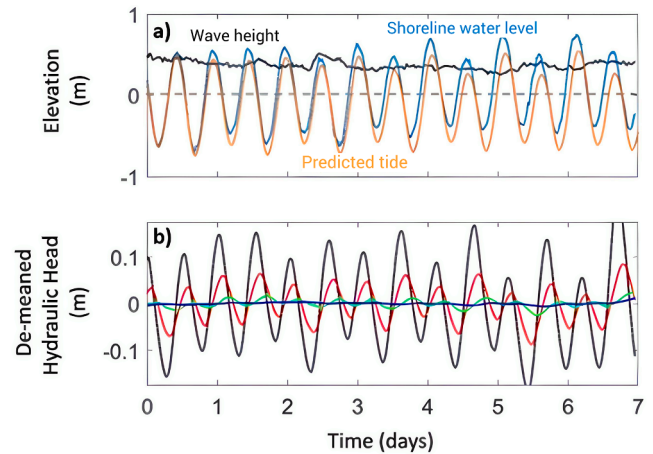

Fig. 2. a) Offshore (26-m water depth) significant wave height (black curve), predicated tidal level (orange curve, NOAA buoy 8651371) and shoreline water level (blue curve, including tides, storm surge, and setup) and b) demeaned freshwater equivalent head (x = 0, 30, 95, and 160 m are black, red, green, and blue curves, respectively) versus time during calm conditions (July 2016). (For interpretation of the references to color in this figure legend, the reader is referred to the web version of this article.)

and that storm surge is up to about 1 m (not shown). Differences between spring and neap tidal ranges are<0.2 m (spring-neap groundwater fluctuations are much smaller than diurnal, semi-diurnal, and storm-driven fluctuations). Significant wave heights (H_s, 4 times the standard deviation of sea-surface elevation fluctuations in the frequency range from 0.05 to 0.30 Hz) recorded every 30 min in 26-m water depth (NDBC station **44100**) ranged from near 0 to 6 m (Fig. 2 is during a calm summer period), with an average of about 1 m. Wave energy in the north

Atlantic Ocean varies seasonally, and often is largest during the fall and winter. Breaking waves in shallow water cause an increase of the shoreline water levels (setup) ranging from about 0.2 to 0.3 times the offshore significant wave height, depending on the offshore bathymetry (da Silva et al., 2020; Guza and Thornton, 1981; Holman and Sallenger, 1985; Lentz and Raubenheimer, 1999; Nielsen, 1988; Raubenheimer et al., 2001; Stockdon et al., 2006 and references therein). Here, setup is estimated to be $0.2H_s$, roughly consistent with observations from a LIDAR on the dune about 300 m north of the wells. Ocean salinity ranged from 24 to 34 PSU. Tidal effects are negligible in the sound and salinities are<2 to 3 PSU (Mulligan et al., 2014). Hydraulic head fluctuations driven by changes in the sound level attenuate before mid-island and do not affect the heads on the ocean-side of the island (Housego, 2021). Precipitation typically is<0.05 m over any 24-hr period, with a resulting water table increase of approximately 3 times the amount of rainfall, and thus<0.15 m (Housego et al., 2021). Precipitation is approximately uniform throughout the year.

Storms are defined as events with combined 36-hr averaged (de-tided) surge and setup exceeding 0.65 m. There were 26 storm events during the 3-year data record, including 4 hurricanes that passed offshore (Hurricanes Joaquin Oct. 2015, Irma Sep. 2017, Jose Sep. 2017, and Maria Sep. 2017) with minimal rainfall (<0.05 m).

During calm conditions ($H_s < \sim 2$ m), the shoreline water level can be approximated with the dominant tidal constituents (primarily M2, S2, N2, O1, K1 (NOAA buoy 865170)) (Fig. 2a). Under these conditions, tides are the dominant driver of fluctuations in the groundwater, with semi-diurnal amplitudes of approximately 0.1 to 0.2 m under the dune crest that attenuate inland (Fig. 2b). During storms, surge and wave-driven setup increase the shoreline water level (by up to almost 2 m during the observation period) above that given by the tidal constituents (Fig. 3a). The resulting storm-generated hydraulic head fluctuations are approximately 1 order of magnitude larger than the tidally driven hydraulic head fluctuations (Fig. 3). The range of the increases in storm-driven head observed at the dune-crest well (x0) is 0.40–1.50 m for the 26 storm events, with the largest increase measured when Hurricane Joaquin passed offshore in Oct 2015. Storm-driven increases in the head levels also attenuate with inland distance, and 160 m inland of the dune (at sensor x160) the maximum increase in head is 0.9 m. Similar to the tidal fluctuations, there are time delays (phase lags) in the occurrences of maximum water levels at each well location as the hydraulic head fluctuation propagates inland (Fig. 3b). The inland propagation speed of the storm driven groundwater levels ranged from 60 to 150 m/day depending on the duration (i.e., the period or frequency) of the elevated ocean water levels.
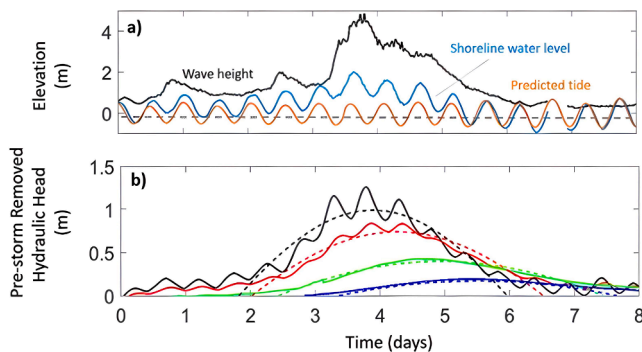

Fig. 3. a) Offshore significant wave height (black curve), predicted tidal level (orange curve (NOAA buoy 8651371)) and shoreline water level (blue curve) and b) observed (solid curves) and sine curve fits ($\omega = 0.72$ d^{-1}, dashed curves) to freshwater equivalent head (x = 0, 30, 95, 160 m are black, red, green, and blue curves, respectively) above the pre-storm levels versus time for a single nor'easter (Sept 2014). (For interpretation of the references to color in this figure legend, the reader is referred to the web version of this article.)

3. Analytical theories

The analytical theories considered here assume a homogeneous, isotropic surface aquifer with uniform saturated hydraulic conductivity K (m/d), specific yield S_y (dimensionless), and constant depth z (m) (bounded below by a horizontal impermeable layer). Capillary effects are neglected. Amplitudes A (m) of hydraulic head fluctuations are assumed small relative to the aquifer depth ($A_{ocean}/z \approx 1/20 \ll 1$). The intertidal region of the relatively steep beach is only about 10 m wide, and the aquifer is assumed to be connected to the ocean by a vertical beach face, which is assumed to be valid inland of the intertidal.

3.1. Linear theory

Assuming further that the aquifer is shallow relative to the wavelength of the hydraulic head fluctuation ($(kz)^2 \ll 1$, where k (m^{-1}) is the wavenumber), and thus that velocities are horizontal and uniform with depth (and that pressures are hydrostatic as in the Dupuit-Forchheimer assumption), Darcy's Law and continuity combine to give the diffusion equation (Ferris, 1951; Jacob, 1950; Nielsen, 1990):

$$\frac{\partial h}{\partial t} = \frac{Kz}{S_y}\frac{\partial^2 h}{\partial x^2} \tag{2}$$

where h (m) is the space and time dependent aquifer head, t (d) is time, and x (m) is the cross-shore coordinate positive inland from the ocean boundary. In this simplified case, the head fluctuation is an inland propagating wave with period τ (d) and exponentially decaying amplitude given by:

$$h(x,t) = A_0 \cos\left(\frac{2\pi}{\tau} - k_i x\right)e^{-k_r x} \tag{3}$$

in which A_0 is the amplitude at the ocean boundary, k_r and k_i are the real and imaginary parts of the complex wavenumber k given by:

$$k = \sqrt{\frac{i2\pi S_y}{\tau K z}} \tag{4}$$

where i is $\sqrt{-1}$. Although according to linear theory $k_i = k_r$, many studies have found discrepancies between these wave number estimates (Erskine, 1991; Fakir and Razack, 2003; Nielsen, 1990; Rotzoll and El-Kadi, 2008; Smith and Hick, 2001; Trefry and Bekele, 2004). If the assumption of small amplitude is relaxed, the solution for $h(x,t)$ includes an overheight and harmonics of the primary fluctuation (both of order $A^2/4z \approx 0.01$ m for this site). Relaxing the vertical beach assumption results in an overheight and harmonics of the order $kA^2\cot\beta$ (≈ 0.1 m) (Nielsen, 1990; Raubenheimer et al., 1999). However, tidal harmonics are several orders of magnitude smaller than diurnal and semi-diurnal fluctuations (Fig. 4a), supporting the assumptions of small amplitude and a vertical beach. The small tidal harmonics are not examined further.

3.2. Higher-Order intermediate depth theories

Deviations from the assumptions of the linear theory, including an inhomogeneous (Trglavcnik et al., 2018) or deep (Nielsen et al., 1997) aquifer, spatially variable aquifer depth (Raubenheimer et al., 1999), capillary effects (Barry et al., 1996; Kong et al., 2013; Li et al., 2000; Shoushtari et al., 2016), large amplitude fluctuations, hysteresis (Cartwright et al., 2005; Nielsen and Perrochet, 2000a,b; Nielsen and Turner, 2000), and a sloping beach (Nielsen, 1990; Raubenheimer et al., 1999) can result in generation of tidal harmonics in groundwater fluctuations or differences between the rate of amplitude attenuation and phase evolution. For a given wave period (τ), the shallow aquifer assumption is valid if $(kz)^2 = S_y\omega z/K < 0.2$, where $\omega = 2\pi/\tau$ is the radian frequency of the fluctuation. Although many of the linear theory assumptions approximately may be valid for the range of hydraulic conductivity (15
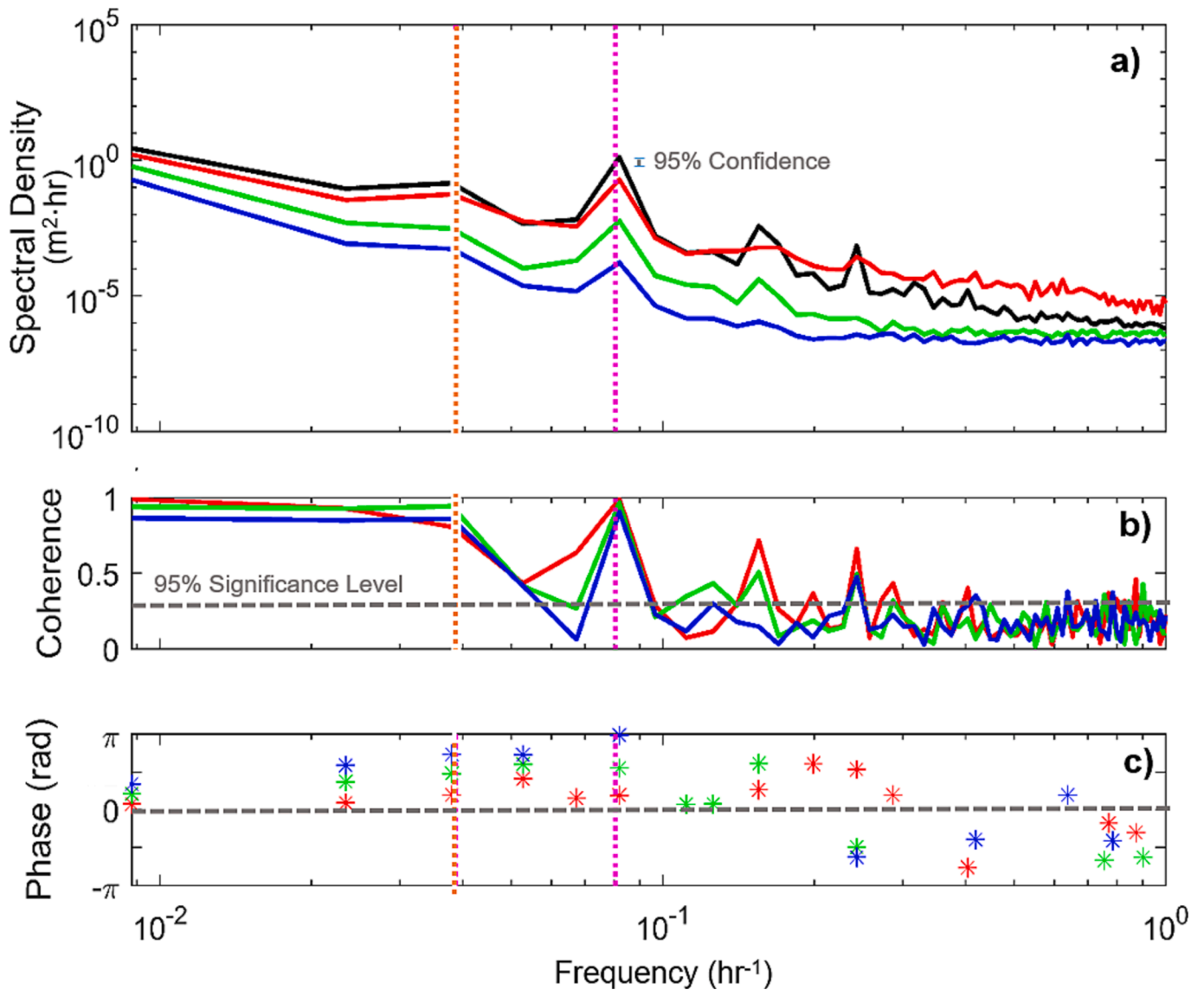
Fig. 4. a) Spectral energy density (m² hr), b) coherence with the signal at x0, and c) phase (radians) shift relative to x0 versus frequency for 70 days of data (50 degrees of freedom). Vertical dotted lines identify the diurnal (orange) and semi-diurnal (magenta) tidal frequencies, and the horizontal dashed line in (b) is the 95% significance level for zero coherence. Wells located at x = 0, 30, 95, 160 m are black, red, green, and blue curves, respectively and correspond to well locations in Fig. 1. (For interpretation of the references to color in this figure legend, the reader is referred to the web version of this article.)

$< K < 90$ m/d) previously estimated at this site, the aquifer depth ($15 < z < 30$ m) violates the shallow aquifer (relative to a wavelength) assumption at tidal frequencies.

As the aquifer depth increases, horizontal velocities become non-uniform with depth and vertical velocities can be significant (Dagan, 1967; Parlange et al., 1984; Fenton, 1990), in contrast with the hydrostatic Dupuit-Forchheimer shallow aquifer assumption. For the small amplitudes considered here, the equations for hydraulic head fluctuations in homogeneous, intermediate depth aquifers, without capillary effects or hysteresis, are to 2nd and infinite order (referred to subsequently as intermediate depth theory), respectively, given by Nielsen et al. (1997):

$$\frac{\partial h}{\partial t} = \frac{Kz}{S_y}\left(\frac{\partial^2 h}{\partial x^2} + \frac{z^2}{3}\frac{\partial^4 h}{\partial x^4}\right) \tag{5}$$

and

$$\frac{\partial h}{\partial t} = \frac{Kz}{S_y}\left(\tan\left(z\frac{\partial}{\partial x}\right)\frac{\partial h}{\partial x}\right) \tag{6}$$

where h is the surface displacement (with $h \ll z$). Similar to linear theory, the solution for the head fluctuation is an inland propagating wave with exponentially decaying amplitude (Eq. (3)). However, the amplitude decay rate and phase evolution, given by the real and imaginary parts of the wavenumber, respectively, no longer are equal ($k_r > k_i$), with the 2nd- and infinite-order dispersion relationships given by:

$$kz = \sqrt{\frac{3}{2}}\sqrt{-1 + \sqrt{1 + \frac{4iS_y\omega z}{3K}}} \tag{7}$$

and

$$kz\tan kz = \frac{iS_y\omega z}{K} \tag{8}$$

The 2nd-order approximation is valid for $S_y\omega z/K < 1.0$. As $S_y\omega z/K \to \infty$, the infinite-order theory predicts that the amplitude attenuation rate will asymptote to $\pi/2z$ and there will be zero phase lag.

Intermediate depth theory also predicts that oscillations near the bottom of the aquifer have slightly larger amplitudes than, and lead the oscillations near the surface, with the vertical variation of the phase ϕ

with depth given by Nielsen et al. (1997):

$$\phi(x, d) = \phi(x, 0) + Arg\{i\sin(k_i d) + \cos(k_r d)\} \qquad (9)$$

where d is distance above the bottom of the aquifer.

This theory does not include capillary effects nor other unsaturated zone processes that are important for the propagation of hydraulic head fluctuations when the height of the capillary fringe is large or when the oceanic fluctuations occur at high frequencies (Li et al., 1997). Additionally, variable specific yields are needed to account for beach filling and draining (infiltration and exfiltration) processes at the beach face (Robinson et al., 1999; Boufadel 2000; Naba et al., 2002). However, the capillary fringe is small in the sandy beach where the data were collected, the storm and tidal fluctuation periods are relatively long, and the analysis is focused inland of the dune crest, which is ∼ 10 m inland of the intersection of the beach with the highest storm-driven ocean water level, and more than ∼ 50 m inland of the calm period ocean-beach intersection. Thus, neglecting capillarity and hysteresis is believed to be an appropriate assumption here.

3.3. Data processing for theory evaluation

Diurnal and semi-diurnal tidal amplitude attenuation and phase lag relative to observations at the x0 well are calculated from spectral analysis (Fig. 4, Geng and Boufadel, 2017; Raubenheimer et al., 1999; Shih 2018; Turner et al., 1998). The 3-yr data record is divided into 15 subsamples, each with 10,240 data points (∼70 days each). Each sub-sample is then broken into ensemble sections of 2048 data points (∼14 days) with 75% overlap. Each ensemble section is de-meaned and quadratically detrended to remove low-frequency oscillations, such as seasonal trends, and tapered with a Hamming window to remove ringing artifacts. Five frequency bands are merged to increase the degrees of freedom. The resulting auto-spectra have 50 degrees of freedom (DOF) and a 0.0146 hr^{-1} bandwidth (Δf). The co-spectrum between time series collected at different locations is used to estimate the signal coherence and phase lags (Geng and Boufadel, 2017). Spectral density (S_d) and phase differences are obtained from the band containing the frequency of each tidal constituent (vertical orange and magenta lines, Fig. 4). Similar to prior spectral analyses of groundwater fluctuations in beaches, peaks in the spectra coincide with the dominant tidal constituents (M2, K1) (Raubenheimer et al., 1999; Geng and Boufadel, 2017). Amplitude is determined from the spectral density of the auto-spectra at each location as $A = \sqrt{2 S_d \Delta f}$. The observed auto-spectral densities at the tidal frequencies are of comparable magnitude to spectral levels estimated in other studies of sandy beaches (Raubenheimer et al., 1999) and are several orders of magnitude smaller than those observed in gravel beaches with much higher hydraulic conductivities (Geng and Boufadel, 2017).

Coherence between the hydraulic head fluctuations at the x0 well and all three inland locations is significant at the 95% confidence level for the semi-diurnal and diurnal tides for 5 of the 15 subsamples and all 5 of these subsamples are for time periods between the months of May and September. The five subsamples with significant coherence levels are for time periods during spring and summer months when offshore wave heights typically are small (<2 m on average). Low coherences could be owing to winter storms that are not well represented by sine waves and cause "noise" at a wide range of frequencies, or by brief, heavy impulse-like precipitation events (often not associated with storm surges) that could put apparent energy into all frequencies, and thus would decrease coherence levels. Leakage into higher frequencies from the spring-neap cycle, which is not well resolved in the 14-day ensemble sections, evapotranspiration (also acts at diurnal periods) and from other low-frequency fluctuations that could not be removed completely by detrending, also may obscure the tidal signals. Thus, only the five 70-day-long subsamples with significant coherence levels at the diurnal and semi-diurnal tidal frequencies at all three inland locations are

considered.

Although storm-driven groundwater fluctuations may be represented well as a pulse (Housego et al., 2021; Li et al., 2004; Trglavcnik et al., 2018), here a sine wave approximation is used for comparison with the theories, the tidal fluctuations, and prior studies (Rotzoll and El-Kadi, 2008). Storm amplitude attenuation and phase lag are determined by fitting a sine curve to the 36-hr average hydraulic head after removing the pre-storm head level at each well (Fig. 3b). The amplitude A of the fit is specified to be the maximum observed 36-hr average head level at each location, the frequency (period) is determined by the best fit at the x0 well, and the phase lag $\Delta(\phi)$ is estimated as the time difference of the maximum head at each location from that at the x0 well normalized by the period. Fit agreements are better for storms where the rise and subsequent fall of the shoreline water level is approximately symmetric in time. Additionally, the same frequency is used at all well locations, so the fit agreement is better at x0 and x30 because the duration of the hydraulic head fluctuation increases with inland distance owing to dispersion. Despite these limitations, the sine curve fits have correlations of R^2 > 0.7 at all well locations for all storms. Storms associated with heavy precipitation are not included in the analysis because the precipitation drives a simultaneous increase in head at all well locations.

Both the storm and the tide data are analyzed relative to the x0 well to avoid effects of changes in the beach and dune topography. During the observation period there were no large scale changes in topography inland of the dune. However, the ocean-side of the dune eroded ∼ 10 m, and the beach profile evolved substantially. Changes in beach morphology create variability in the attenuation distance between the ocean and the x0 well, as well as variation in wave set-up and run-up processes at the coast. These morphologic changes also may alter the effect of the capillary processes, which play a stronger role in modifying the hydraulic head fluctuations where the beach is sloped (Li et al., 1997; Geng and Boufadel, 2017). The amplitudes estimated for the storm surges at the ocean and x0 well also are affected by the tidal stage of the storm and the pre-storm head level. Consequently, relationships of hydraulic head fluctuations between the inland wells (Fig. 5, black, red and green circles) are more consistent (smaller standard deviation of the amplitude ratio) than those between the ocean and the well closest to the ocean (x0) (Fig. 5, blue circles are more scattered about the 1:1 line than the other circles are). Furthermore, the estimated surge amplitude at the x0 well sometimes is larger than that at the shoreline (A_{x0}/A_{ocean}
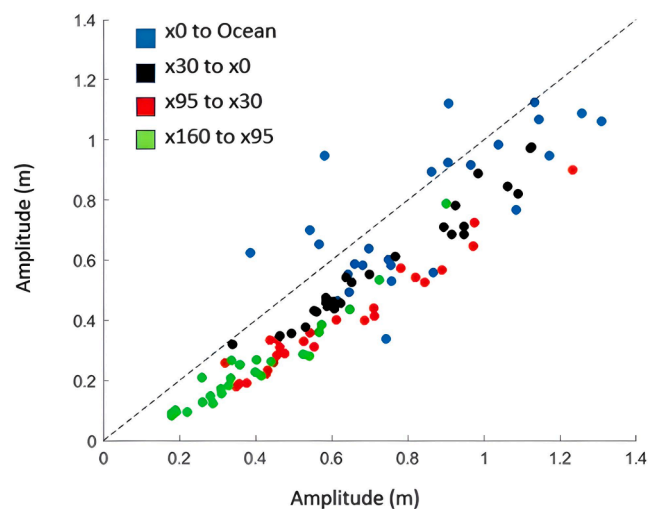

Fig. 5. Hydraulic head amplitude at the x0 (blue), x30 (black) x95 (red), and x160 (green) wells versus the shoreline water level (ocean) and heads at the x0, x30, and x95 wells, respectively. Values below the black dashed 1:1 line indicate amplitudes are decreasing inland. (For interpretation of the references to color in this figure legend, the reader is referred to the web version of this article.)

> 1), highlighting the need for more accurate representations of ocean processes, including setup and runup. Therefore, the propagation of the hydraulic head fluctuations are calculated relative to the x0 well for both the tides and storm surges.

4. Observational estimates of the cross-shore propagation and vertical structure of hydraulic head fluctuations

The real and imaginary wave numbers are computed for the diurnal, semi-diurnal, and storm fluctuations from the best-fit cross-shore trends of amplitude attenuation and phase lag (from Eq. (3)) as:

$$|\ln(\alpha)| = k_r x \qquad (10a)$$

$$|\Delta\phi| = k_i x \qquad (10b)$$

where x (m) is the cross-shore distance from the x0 well, α (non-dimensional) is the amplitude relative to the amplitude at the x0 well (A/A_0), and $\Delta(\phi)$ (rad) is the phase difference relative to the signal at the x0 well.

The logarithms of the tidal and storm amplitude attenuation and the phase lags (Eq. (10)) decrease linearly inland (Fig. 6, $R^2 > 0.9$, Table 1 (tides only)) as expected from theory, and consistent with the assumptions of a homogeneous and isotropic surface aquifer (Nielsen, 1990). The rates (slopes in Table 1, and wavenumbers in Table 2) of amplitude attenuation (k_r) and phase lag evolution (k_i) increase with the frequency of the fluctuation, consistent with the dispersion relation for groundwater waves (Eqs. (4), (7), and (8)). Thus, storm-driven hydraulic head fluctuations propagate more rapidly and attenuate less than the higher-frequency tidal oscillations.

For the individual storms (which have a range of estimated frequencies, $0.20 < \omega < 0.85$), the shallow aquifer parameter $(kz)^2$ is < 0.15 for the estimated aquifer depth $15 < z < 30$ m, satisfying the shallow aquifer assumption (Fig. 7). The storms are consistent with all theories within 95% confidence levels. However, the average storm k_i (0.012 m^{-1}, Table 2) is 50% larger than the average k_r (0.008 m^{-1}, Table 2), in contrast with linear shallow aquifer theory for which $k_r = k_i$, possibly owing to inaccuracies of modeling storms as sine waves. In particular, an analytical theory (Li et al., 2004) suggests that storm-driven fluctuations modeled as a Gaussian pulse propagate faster than those approximated as a sine wave, and thus have a smaller k_i and would be more consistent with linear shallow aquifer theory. The estimated amplitudes and phase lags of storm fluctuations are approximately vertically uniform (consistent with linear shallow aquifer theory, not shown).

For the diurnal and semi-diurnal tidal fluctuations, the wavenumbers estimated from the amplitude attenuation and phase evolution suggest the shallow aquifer assumption may be violated given the estimated aquifer depth range (Fig. 7 and Table 2). Furthermore, consistent with the intermediate depth theories, the tidal fluctuations have more rapid rates for amplitude attenuation (k_r) than the rates for phase lag evolution (k_i). Estimates of k_i and k_r predicted by infinite-order dispersion (Eq. (8)) for $K = 60$ m/d and $z = 20$ m (best fit of infinite-order theory to observations, see Section 5) fall within 1 standard deviation of the observed values for both storms and tides.

For the same fifteen 70-day-long subsamples used for the horizontal propagation analysis the diurnal and semi-diurnal fluctuations below the surface are correlated with those at the surface at the two well clusters closest to the ocean (x0 and x30, the black and red wells in Fig. 1b, c) (Fig. 8b). Depth-dependent variations in tidal amplitudes cannot be resolved (smaller than the 95% confidence limits, Fig. 8a), which is not inconsistent with the higher-order theories. However, consistent with intermediate depth theory (Eq. (9), Nielsen et al., 1997) and with (unpublished) laboratory observations (Nielsen, pers. comm.), the semi-diurnal tidal signal at the deepest location leads the signal at shallower locations (Fig. 9), and the vertical dependence of the phase shift does not depend on cross-shore location (compare Fig. 9a for x0 with Fig. 9b for x30). Differences between the observed and theoretical vertical structure may arise from the sloping beach or vertical salinity structure. The vertically dependent diurnal phase shifts are about half of those for the semi-diurnal tide (Fig. 8c), consistent with theory. However, the diurnal phase shifts do not increase monotonically with depth for all fifteen subsamples, in contrast with theory.

The intermediate aquifer estimates do not account for hysteresis, which could cause reduced amplitude attenuation and phase lag evolution with increasing period (Cartwright, 2014; Shoushtari et al., 2015; Werner and Lockington, 2003), crudely consistent with the observations. However, analytical theories including hysteresis (or capillarity) (Shoushtari et al., 2016) predict larger ratios of real to imaginary wavenumbers than those estimated from the observations (circles in Fig. 7), and dispersion relationships (curves in Fig. 7) that include hysteresis and capillary effects (not shown) would result in poorer agreement with the observations for the range of the estimated geologic parameters ($15 < z < 30$ m and $15 < K < 90$ m/d) (see Appendix). Shorter period tidal harmonics (M4 and M6, Fig. 4a and 8a) are weak, and cannot be used to explore the asymptotic behavior of k_r and k_i with increasing non-dimensional aquifer depth.
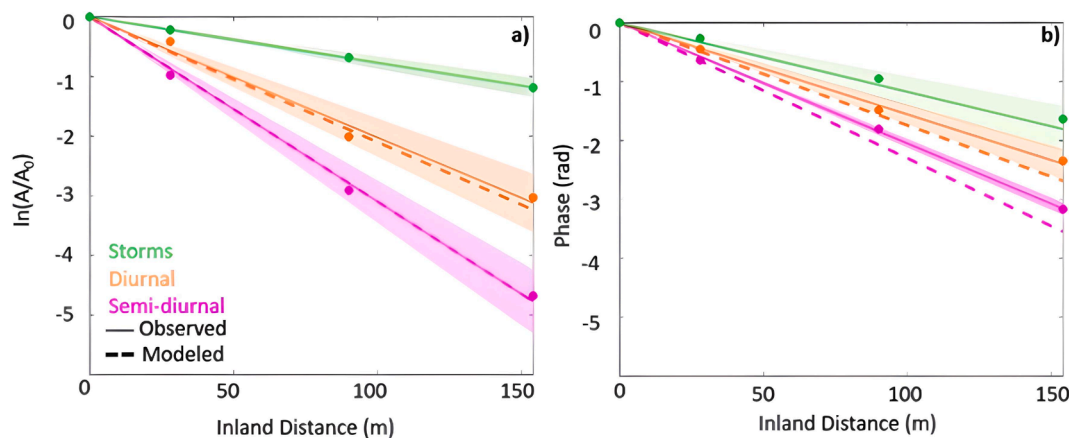

Fig. 6. a) Amplitude attenuation and b) phase lag versus inland distance of storm- (green, n = 26), diurnal- (orange, n = 5), and semi-diurnal- (pink, n = 5) driven groundwater fluctuations. The filled symbols are the mean observed values at each location, the solid lines are the average slope from the least squares linear fits to each set of observations, the shaded areas represent ± 1 standard deviation of the least squares linear fit slopes, and the dashed lines are the model simulations for an aquifer diffusivity of 6000 m^2/d. (For interpretation of the references to color in this figure legend, the reader is referred to the web version of this article.)

Table 1

Slopes and correlations R^2 of least squares fits to tidal amplitude attenuation and phase lag with inland distance, and the slope factor, the ratio of the slope of the phase to the slope of the amplitude fit for that frequency for each of the five 70-day periods with high correlations.

Amplitude				Phase				Slope Factor	
Diurnal		Semi-diurnal		Diurnal		Semi-diurnal			
Slope	R^2	Slope	R^2	Slope	R^2	Slope	R^2	Diurnal	Semi-diurnal
−0.0215	0.918	−0.0306	0.995	−0.0137	0.936	−0.0205	0.999	0.64	0.67
−0.019	0.975	−0.0295	0.996	−0.0156	0.959	−0.0200	0.998	0.82	0.68
−0.0198	0.853	−0.0326	0.986	−0.0167	0.988	−0.0200	0.996	0.84	0.61
−0.0237	0.992	−0.0347	0.994	−0.0169	0.999	−0.0211	0.998	0.71	0.61
−0.0172	0.973	−0.0276	0.996	−0.0149	0.998	−0.0209	0.997	0.87	0.76

Table 2

Average estimated wave numbers (n = number of storm events or 70-day-long tidal records averaged).

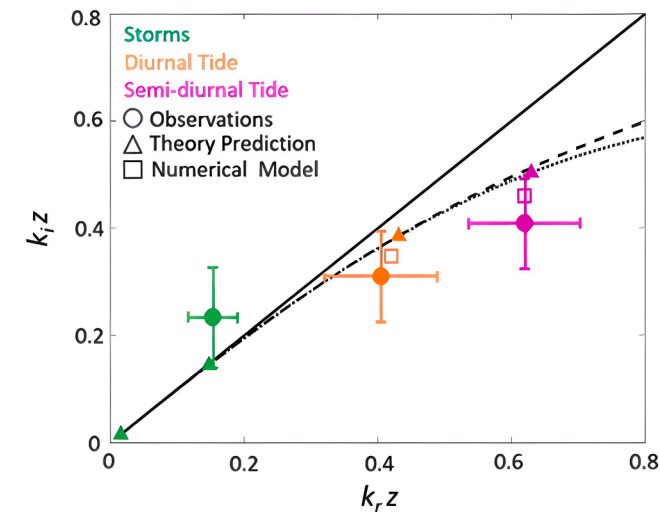| k_r			k_i		
Storms (n = 26)	Diurnal (n = 5)	Semi-diurnal (n = 5)	Storms (n = 26)	Diurnal (n = 5)	Semi-diurnal (n = 5)
0.008	0.020	0.031	0.012	0.016	0.021

Fig. 7. Imaginary versus real component of the wave number scaled by aquifer depth (using $z = 20$ m) estimated from observations (filled circles), simulations (open squares), and intermediate depth theory (filled triangles, Eq. (7)) for the storm (green), diurnal (orange), and semi-diurnal (magenta) propagation. The curves represent the linear (solid black, Eq. (4)), 2nd-order (dashed black, Eq. (7)), and infinite-order (dotted black, Eq. (8)) in depth, small-amplitude dispersion relations. Bars on the observed estimates represent ± 1 standard deviation of the observational estimates (shaded areas in Fig. 6) Theoretical estimates for storms (green triangles) are given for the largest and smallest observed periods. The numerical and theoretical values assume $S_y = 0.2$ based on site characterization and $K = 60$ m/d based on a fit to the observations. (For interpretation of the references to color in this figure legend, the reader is referred to the web version of this article.)

Fig. 8. a) Spectral energy density (m^2 hr), b) coherence with the signal at the shallowest well (-1 m), and c) phase shift relative to the shallowest well versus frequency for all wells at the x0 site. Dotted vertical lines identify the diurnal (orange) and semi-diurnal (magenta) tidal frequencies, and the horizontal dashed line in (b) is the 95% significance level for zero coherence. Color key for well depths is given in (a). (For interpretation of the references to color in this figure legend, the reader is referred to the web version of this article.)

5. Numerical simulations for a homogeneous, intermediate depth aquifer

The interpretation of the field observations is examined further by using an idealized uniform density groundwater transport model (MODFLOW-NWT (Niswonger et al., 2011)) with assumptions consistent with the analytical theories (neglecting capillarity, hysteresis, variable density, and vertical layering) to simulate tidal groundwater fluctuations in a constant depth, homogeneous, isotropic surface aquifer without a capillary fringe. The 2-dimensional model domain represents
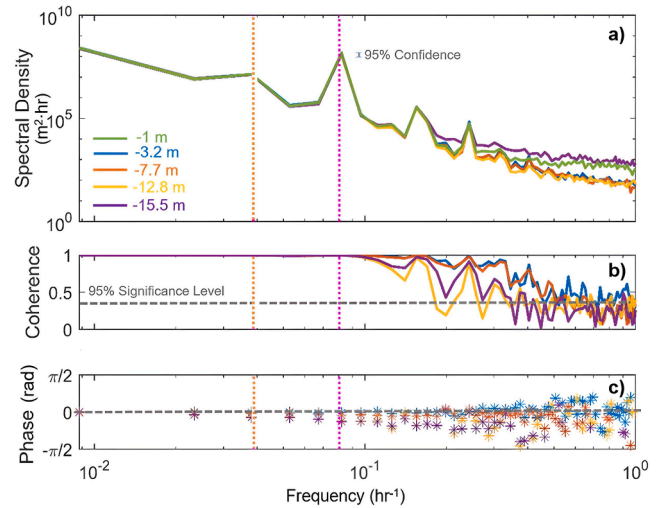
a vertical cross-section that extends from 200 m inland to 250 m offshore of the dune (Fig. 10). The observed ocean beach configuration varied significantly over the 3-year field study owing to erosion and accretion. Rather than using a snapshot of a single beach state, the beach is approximated as linear with a 0.1 slope. The vertical grid resolution ranges from 0.1 to 1.0 m from the surface to the bottom, and the horizontal resolution ranges from 0.1 to 5.0 m, with the highest resolution along the beach face, similar to prior studies (Heiss and Michael, 2014; Mulligan et al., 2011; Robinson et al., 2007, 2014). The hydrogeologic parameters ($z = 20$ m, $S_y = 0.2$) are based on geologic characterizations of the region and the observed propagation of the tide and storm fluctuations. In particular, using the above estimated 20-m aquifer depth and specific yield, the hydraulic conductivity that yields the best match between theory and observations (smallest percent error between measurement and theory prediction) for all fluctuation periods is $K = 60$ m/day ($D = 6000$ m^2/d), consistent with previous estimates at this site (Turner and Masselink, 1998). A model run including vertical anisotropy (K_x:K_z = 10:1) yields the same propagation results for storms and tides as the isotropic runs. Variable-density effects are not expected to extend inland of the intertidal (see Section 6.2).

No-flow boundaries are applied at the bottom of the model domain and at the vertical ocean boundary. Inland of the beach the elevation of the top of the model domain is above the maximum height of the simulated water table (no exchange across the top horizontal boundary). Significant seepage face development is not expected (and was not observed) for this steep beach slope (β = 0.1), and is neglected at the
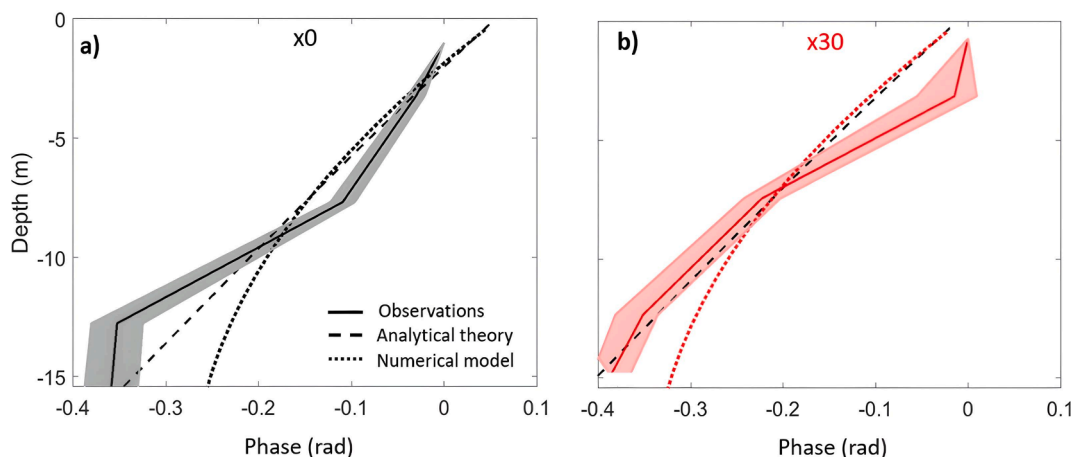
Fig. 9. Phase (horizontal axis) relative to the shallowest well as a function of depth (vertical axis) at a) x0 and b) x30 for semi-diurnal tidal fluctuations. Shaded regions represent the 95% confidence interval based on the range of measured estimates across all subsamples, dotted curves are the phase differences from the numerical model, and dashed black lines are the theoretical profiles (Nielsen et al., 1997).
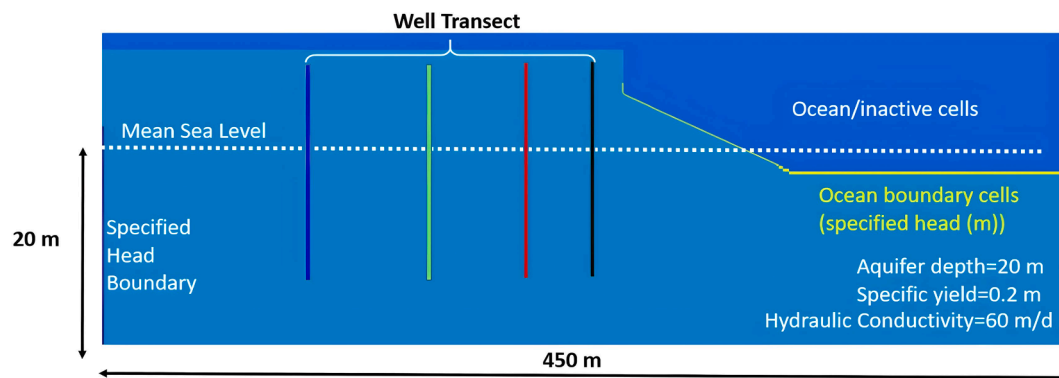

Fig. 10. Schematic of the model domain.

model shoreline. MODFLOW-NWT includes the nonlinearity associated with wetting and drying processes (Bedekar et al., 2012; Hunt and Feinstein, 2012). Specifically, rewetting occurs when when heads in adjacent cells are expected to direct flow into the currently dry cell using an upstream weighted approach and the resulting water table position exceeds the bottom elevation of the cell (Niswonger et al., 2011) For wetting and drying processes, the thickness factor (THICKFACT) was specified as 0.001 and a correction was applied to the hydraulic head relative to the cell-bottom altitude if the cell is surrounded by dewatered cells (IBOTAV = 1) (Niswonger et al., 2011). Tidal fluctuations attenuate prior to reaching the inland boundary (fluctuation amplitude < 0.001 m), where a Dirichlet boundary is applied. The landward Dirichlet boundary is set to 0.7 m based on extrapolating the average observed head gradient to the inland model boundary and is consistent with the inland water table elevation measured by a well at the center of the island (not shown, located at x ~ 300 m, annual mean 0.76 ± 0.4 m). At the ocean-side boundary, the model is driven with 0.5-m amplitude (i) semi-diurnal and (ii) diurnal tides using time series of mean shoreline water levels (average over 15 min) with a modified version of the wave-PBC package (Rakhimbekova et al., 2022).

Semi-diurnal and diurnal tidal simulations were each run for 30 days, including a 7-day spin-up period. Head data were extracted at a depth of −5 m (which overlaps with the depth of well screens) every 5 m in the cross-shore, at and onshore of the position of the x0 well. Head data also were extracted every 1 m in the vertical extending from $z = 0$ m to $z = -15$ m NAVD88 (maximum well depth) at the position of the x0 and x30 wells. Amplitudes and phases were estimated from quadratically detrended head data using a least squares fit to sine waves. The

head fluctuation is too small to be resolved at locations > 90 m inland of the x0 well.

The cross-shore propagation of simulated tidal fluctuations without capillary effects, hysteresis, or vertical layering is similar to the observed behavior. Specifically, the logarithm of the modeled amplitude attenuation is similar to that for the observations (Fig. 6, compare dashed with solid lines). In addition, consistent with the observations (and with the intermediate depth theory), the slope of the simulated tidal phase lags with inland distance is smaller than that for the amplitude attenuation (compare dashed orange and pink lines in Fig. 6b with those in Fig. 6). Discrepancies between the observed and simulated phase lags increase with inland distance, at least partly owing to difficulties fitting curves to the simulated hydraulic head fluctuations that become small as the signal attenuates inland. Additional sensitivity runs that varied hydraulic conductivity ($z = 20$ m K = 15 m/d, 90 m/d) and aquifer depth ($z = 15$, 30 m K = 60 m/d) also had smaller rates of phase lag relative to the tidal amplitude attenuation with inland distance. Model runs with inland heads of 0, 1, and 2 m showed that the tidal propagation was not sensitive to the inland head level, suggesting that seasonal or inter-annual variations in inland heads do not alter the tidal propagation (see Appendix). The direction of the observed relationship between the phase lag and tidal amplitude attenuation is reproduced with MODFLOW-NWT for the estimated range of geologic parameters without capillarity or hysteresis, suggesting that aquifer depth is likely the primary cause of the difference between the phase lag and tidal amplitude attenuation in the water table fluctuations measured at Duck inland of the dune.

The simulated vertical phase structure also is similar to the observed

structure and to that expected from the intermediate depth theory for $0 > d > -10$ m at both x0 and x30 (Fig. 9). Similar to the model-data differences in the cross-shore propagation, discrepancies between the observed and modeled vertical phase structure partly may be owing to difficulties fitting curves to the simulated hydraulic head fluctuations. The agreement of the simulated and observed cross-shore and vertical structure of hydraulic head fluctuations suggests they can be predicted inland of the beach without including computationally expensive simulations of capillarity, hysteresis, or vertical layering.

6. Discussion

6.1. Estimating aquifer properties from ocean-driven head fluctuations

Linear shallow aquifer theory and observations of ocean-forced hydraulic head fluctuations have been used to estimate coastal-surface-aquifer diffusivity and to characterize regional aquifer structure (Erskine, 1991; Fakir and Razack, 2003; Nielsen, 1990; Rotzoll and El-Kadi, 2008; Smith and Hick, 2001; Trefry and Bekele, 2004, and many others). Specifically, from (3) and (4) the diffusivity D, defined as Kz/S_y, can be estimated from the inland amplitude attenuation rate or phase lag as:

$$D_{amp} = \frac{\pi}{\tau} \frac{x^2}{(\ln(a))^2} \tag{11a}$$

$$D_{phase} = \frac{\pi}{\tau} \frac{x^2}{(\Delta\varphi)^2} \tag{11b}$$

The tidal amplitude-based diffusivity estimates (average diurnal and semi-diurnal D_{amp} are 8000 and 6000 m²/d, respectively) are roughly consistent with the storm-based estimates ($D_{amp} = 6000$ m²/d). However, the tidal phase-based diffusivity estimates are larger than would be expected based on the theories (average diurnal and semi-diurnal D_{phase} are 13,000 and 9000 m²/d, respectively), and are at the high end of the values expected from the estimated hydrogeological parameters. The values for amplitude- and phase-based diffusivity often are averaged to obtain a final linear-theory estimate for aquifer diffusivity. The resulting estimates for this system are ~ 11000 (based on the propagation of the diurnal tide) and ~ 8000 m²/d (semi-diurnal tide), which are larger than that estimated from the storm propagation (7000 m²/d). Diffusivities estimated from the numerical simulations, in which D is set to be 6000 m²/d, are similar to those for the observed diurnal ($D_{amp} = 7000$, $D_{phase} = 11000$ m²/d) and semi-diurnal ($D_{amp} = 7000$, $D_{phase} = 10000$ m²/d) tidal fluctuations.

These inconsistent amplitude and phase diffusivity estimates may be owing to violations of the shallow aquifer assumption, suggesting that it is important to determine whether the surface aquifer meets the shallow aquifer criterion ($(kz)^2 = S_y\omega z/K \ll 1$) before using the Jacob-Ferris model to estimate aquifer properties. Similar aquifer characterization approaches can be applied in intermediate depth aquifers. If the aquifer is approximately homogeneous and the logarithm of the tidal amplitude attenuation and the phase evolution are linear with inland distance, diffusivity can be estimated by identifying the hydrologic parameters that yield the best fit to intermediate depth theory. Here, the combinations of K and z that give the best fit to the wavenumbers (or diffusivities) estimated from the observed amplitude attenuation and phase evolution for the semi-diurnal tide correspond to D=~4000–10000 m²/d (Fig. 11, consistent with prior estimates at Duck.

Based on this analysis, it is recommended to collect hydraulic head measurements by sampling (every 15 min or so) for ~ 70 days to provide 140 and 70 cycles of the semi-diurnal and diurnal tidal constituents, respectively. Windowing the data to remove low-frequency leakage, and frequency merging or ensemble averaging short sections of data (with about 75% overlap) to attain about 50 degrees of freedom also is recommended.
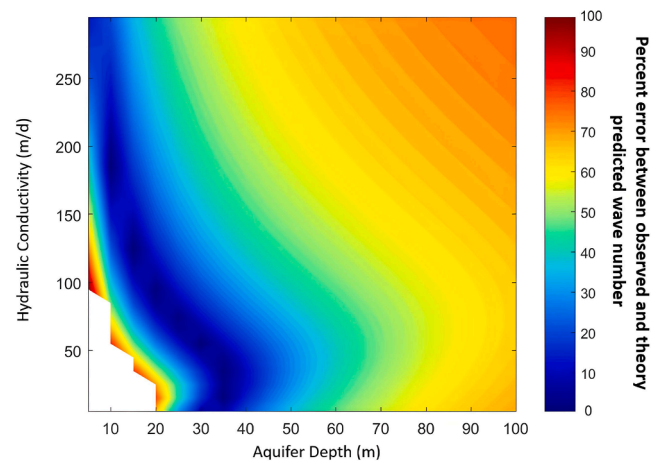

Fig. 11. Magnitude of the difference between the wave number ($k = k_r + k_i$) estimated from observations and from intermediate depth theory (Eq. (7), colors, scale on the right) normalized by the observational estimates as a function of hydraulic conductivity and aquifer depth (assuming $S_y = 0.2$) for semi-diurnal tides ($|k_{theory} - k_{observed}|/k_{observed}$ for each K, z combination). Estimated parameters used for intermediate depth theory (Section 4) also included errors for diurnal tides and storms (not shown).

Other processes and environmental factors such as capillarity, vertical layering, and variable aquifer depths also can generate differences in the inland evolution of amplitudes and phases, and thus can result in different amplitude- and phase-based linear theory diffusivity estimates (Cartwright et al., 2005; Erskine, 1991; Fakir and Razack, 2003; Nielsen et al., 1997; Raubenheimer et al., 1999; Shoushtari et al., 2015; Smith and Hick, 2001; Trefry and Bekele, 2004; Trefry and Johnston, 1998). Furthermore, if there is complex stratigraphy or leakage between layers, the propagation analysis will not yield a linear trend (Jiao and Tang, 1999; Trglavcnik et al., 2018). Consequently, it is important to consider both the depth regime and geologic environment when applying ocean-driven hydraulic head fluctuation propagation to estimate aquifer parameters.

6.2. Inland heads, saline plumes, and estimating hydraulic head fluctuations

Scatter in the observed propagation of hydraulic head fluctuations driven by ocean processes also may result from violations of other assumptions used to derive the dispersion relationships. As discussed above, including the neglected effects of capillarity and hysteresis on wave propagation (Barry et al., 1996; Cartwright et al., 2005; Li et al., 1997; Shoushtari et al., 2015) does not lead to better estimates of wavenumbers. Although the model fails to account for the temporal asymmetry of beach filling and draining (the beach fills more rapidly than it drains), these effects are expected to be confined primarily to the intertidal region.

Seasonal variations in recharge (rainfall), storm events, and sound (bay) water levels may influence the inland (mid-island) hydraulic head-level and subsurface salinity structure (Heiss and Michael, 2014; Robinson et al., 2014), potentially creating temporal and spatial variations in the effective aquifer depth that may modify tidal- and storm-driven head fluctuations. The variation in inland heads (<2 m range) owing to these annual, seasonal, and storm processes is small relative to the aquifer depth (~20 m), and numerical model results are insensitive to inland head levels (Dirichlet boundary condition) set to 0, 1 (5% increase in aquifer depth), and 2 m (10% increase) (see Appendix). However, estimates of fluctuation amplitudes can be sensitive to initial head distributions, which affect the minimum head levels. Specifically, ocean fluctuations primarily determine the maximum head level, so high initial inland heads result in smaller overall fluctuations, which can

lead to underestimation of amplitudes and overestimation of attenuation rates.

Neither the analytical nor the numerical model include density effects. Although density gradients between the ocean and fresher terrestrially derived groundwater play an important role in groundwater dynamics at the aquifer-ocean interface, density gradients most strongly impact circulation and pressure gradients in the intertidal (Abarca et al., 2013; Heiss and Michael, 2014; Robinson et al., 2006, 2007, 2014; Xin et al., 2010), and effects inland of the dune are expected to be small. Plumes of saline water were measured at the x0 and x30 wells following several of the larger storms, and corresponding changes in the subsurface salinity structure could contribute to some of the variance in storm-period head fluctuations. At the x0 well there were 8 instances of high salinity water (max salinity 23–32 PSU) in the aquifer after ocean surge events that persisted from 13 h to 23 days. The x30 well also showed increases in salinity after two of the storm events (max salinity 12 PSU), but the plumes lasted for only $\sim$ 2 days. Apart from these two events there was little salinity variation at the x30 well (annual average salinity 6.80 $\pm$ 1.00 PSU. At the two most inland wells salinities are constant throughout the observation period (x95 annual average salinity 1.90 $\pm$ 0.90 PSU, x160 annual average salinity 0.14 $\pm$ 0.02 PSU). The tidal analysis is based on data collected between May and September when there were no large storms or salinity variations.

7. Conclusions

Three years of observations of ocean water levels and hydraulic heads in an approximately 20-m-deep barrier island surface aquifer were used to evaluate analytical theories for inland propagation of ocean shoreline fluctuations. The logarithm of the amplitude attenuation and the phase lag evolution for semi-diurnal-, diurnal-, and storm-driven fluctuations vary linearly with inland distance at rates increasing with fluctuation frequency (e.g., tides attenuate more rapidly than the longer-duration storm fluctuations), as expected for the approximately homogeneous aquifer. A theory for small amplitude fluctuations in intermediate depth aquifers that previously has not been compared with field data is shown to reproduce the observed differences between the tidal amplitude attenuation and phase lag rates. In addition, tidal fluctuations near the surface of the aquifer lag those near the bottom, as predicted by the intermediate depth aquifer theory. In contrast, the propagation of longer-period (lower frequency) storm-induced increases in ocean water levels is consistent with small amplitude, shallow aquifer (linear) theory. Numerical model simulations support the conclusion that the cross-shore and vertical structure of tidal fluctuations may result primarily from nonlinear effects of an intermediate depth aquifer.

Diffusivity estimates based on propagation of tidal groundwater fluctuations and small amplitude, linear shallow aquifer theory (Jacob-Ferris model) are larger than those based on the storm fluctuations, and tidal amplitude-based estimates are smaller than tidal phase-based estimates, similar to many prior results. However, diffusivities estimated from amplitude and phase evolution for tides and storms using intermediate depth theory are roughly consistent with each other, suggesting that large-scale aquifer properties can be estimated from fluctuations driven by ocean water-level changes using the appropriate theory. These results also suggest that the appropriate analytical theory can be used to estimate the maximum water table elevation in response to tide-and-surge forcings in hydrogeologic settings, where the aquifer depth is approximately constant and the sediments are approximately homogeneous.

CRediT authorship contribution statement

Rachel Housego: Funding acquisition, Conceptualization, Methodology, Formal analysis, Visualization, Writing – original draft. **Britt Raubenheimer:** Funding acquisition, Conceptualization, Methodology, Supervision, Writing – review & editing. **Steve Elgar:** Funding acquisition, Conceptualization, Methodology, Supervision, Writing – review & editing. **Ming Zhi Wu:** Conceptualization, Methodology, Writing – review & editing.

Declaration of Competing Interest

The authors declare that they have no known competing financial interests or personal relationships that could have appeared to influence the work reported in this paper.

Data availability

Data is linked at the end of the article

Appendix A. Supplementary data

Supplementary data to this article can be found online at https://doi.org/10.1016/j.jhydrol.2023.130017.

References

Abarca, E., Karam, H., Hemond, H., Harvey, C., 2013. Transient groundwater dynamics in a coastal aquifer: The effects of tides, the lunar cycle, and the beach profile. Water Resour. Res. 49 (5), 2473–2488. https://doi.org/10.1002/wrcr.20075.

Anderson, W.P.J., Lauer, R.M., 2008. The role of overwash in the evolution of mixing zone morphology within barrier islands. Hydrogeol. J. 16 (8), 1483–1495. https://doi.org/10.1007/s10040-008-0340-z.

Bakhtyar, R., Brovelli, A., Barry, D.A., Robinson, C., Li, L., 2013. Transport of variable-density solute plumes in beach aquifers in response to oceanic forcing. Adv. Water Resour. 53, 208–224. https://doi.org/10.1016/J.ADVWATRES.2012.11.009.

Barry, D.A., Barry, S.J., Parlange, J.Y., 1996. Capillarity correction to periodic solutions of the shallow flow approximation. Coast. Estuar. Stud. 50, 496–510. https://doi.org/10.1029/CE050p0496.

Bedekar, V., Niswonger, R.G., Kipp, K., Panday, S., Tonkin, M., 2012. Approaches to the simulation of unconfined flow and perched groundwater flow in MODFLOW. Groundwater 50 (2), 187–198.

Befus, K.M., Barnard, P.L., Hoover, D.J., Finzi Hart, J.A., Voss, C.I., 2020. Increasing threat of coastal groundwater hazards from sea-level rise in California. Nat. Clim. Chang. 10 (10), 946–952.

Boufadel, M.C., 2000. A mechanistic study of nonlinear solute transport in a groundwater–surface water system under steady state and transient hydraulic conditions. Water Resour. Res. 36 (9), 2549–2565.

Boufadel, M.C., Li, H., Suidan, M.T., Venosa, A.D., 2007. Tracer studies in a laboratory beach subjected to waves. J. Environ. Eng. 133 (7), 722–732. https://doi.org/10.1061/(ASCE)0733-9372(2007)133:7(722).

Browder, A.G., McNinch, J.E., 2006. Linking framework geology and nearshore morphology: Correlation of paleo-channels with shore-oblique sandbars and gravel outcrops. Mar. Geol. 231 (1–4), 141–162. https://doi.org/10.1016/j.margeo.2006.06.006.

Carr, P.A., Van Der Kamp, G.S., 1969. Determining aquifer characteristics by the tidal method. Water Resour. Res. 5 (5), 1023–1031.

Cartwright, N., 2014. Moisture-pressure dynamics above an oscillating water table. J. Hydrol. 512, 442–446.

Cartwright, N., & Gibbes, B. (2011), Oceanic pulse forcing of a beach groundwater system. In *Coasts and Ports 2011 : Diverse and Developing: Proceedings of the 20th Australasian Coastal and Ocean Engineering Conference and the 13th Australasian Port and Harbour Conference.* 140. Engineers Australia.

Cartwright, N., Nielsen, P., Li, L., 2004. Experimental observations of watertable waves in an unconfined aquifer with a sloping boundary. Adv. Water Resour. 27 (10), 991–1004. https://doi.org/10.1016/J.ADVWATRES.2004.08.006.

Cartwright, N., Nielsen, P., Perrochet, P., 2005. Influence of capillarity on a simple harmonic oscillating water table: Sand column experiments and modeling. Water Resour. Res. 41 (8) https://doi.org/10.1029/2005WR004023.

Chardón-Maldonado, P., Pintado-Patiño, J.C., Puleo, J.A., 2016. Advances in swash-zone research: Small-scale hydrodynamic and sediment transport processes. Coast. Eng. 115, 8–25. https://doi.org/10.1016/j.coastaleng.2015.10.008.

Church, P.E., Granato, G.E., 1996. Bias in groundwater data caused by well-bore flow in long-screen wells. Groundwater 34 (2), 262–273. https://doi.org/10.1111/j.1745-6584.1996.tb01886.x.

da Silva, P.G., Coco, G., Garnier, R., Klein, A.H., 2020. On the prediction of runup, setup and swash on beaches. Earth Sci. Rev. 204, 103148.

Dagan, G., 1967. Second-order theory of shallow free-surface flow in porous media. Quart. J. Mech. Appl. Math. 20 (4), 517–526. https://doi.org/10.1093/qjmam/20.4.517.

Elci, A., Molz, F.J., Waldrop, W.R., 2001. Implications of observed and simulated ambient flow in monitoring wells. Groundwater 39 (6), 853–862. https://doi.org/10.1111/j.1745-6584.2001.tb02473.x.

Erskine, A.D., 1991. The effect of tidal fluctuation on a coastal aquifer in the UK. Groundwater 29 (4), 556–562. https://doi.org/10.1111/j.1745-6584.1991.tb00547.x.

Fadili, A., Najib, S., Mehdi, K., Riss, J., Makan, A., Boutayeb, K., Guessir, H., 2016. Hydrochemical features and mineralization processes in coastal groundwater of Oualidia, Morocco. J. Afr. Earth Sci. 116, 233–247.

Fakir, Y., Razack, M., 2003. Hydrodynamic characterization of a Sahelian coastal aquifer using the ocean tide effect (Dridrate Aquifer, Morocco). Hydrol. Sci. J. 48 (3), 441–454. https://doi.org/10.1623/hysj.48.3.441.45281.

Fenton, J. D. (1990). Calculating seepage flow with a free surface: Some old methods and some new ones. *New Zealand Geomechanics Society Groundwater and Seepage Symposium.*

Ferris, J. G. (1951), Cyclic fluctuations of water level as a basis for determining aquifer transmissibility. In: Assemblée générale de Bruxelles, tome II, 148–155. IAHS Publ. no. 33.

Fofonoff, N., & Millard, R.C. Jr. (1983), Algorithms for the computation of fundamental properties of seawater. Paris, France, UNESCO, 53pp. (UNESCO Technical Papers in Marine Sciences; 44), http://hdl.handle.net/11329/109.

Geng, X., Boufadel, M.C., 2017. Spectral responses of gravel beaches to tidal signals. Sci. Rep. 7 (1), 40770.

Grant, A.R.R., Wein, A.M., Befus, K.M., Hart, J.F., Frame, M.T., Volentine, R., et al., 2021. Changes in liquefaction severity in the San Francisco Bay Area with sea-level rise. In: Geo-Extreme 2021, American Society of Civil Engineers, Reston, VA, Vol. 0, 308–317. https://doi.org/10.1061/9780784483695.030.

Guza, R.T., Thornton, E.B., 1981. Wave set-up on a natural beach. J. Geophys. Res. 86 (C5), 4133. https://doi.org/10.1029/JC086iC05p04133.

Heiss, J.W., Michael, H.A., 2014. Saltwater-freshwater mixing dynamics in a sandy beach aquifer over tidal, spring-neap, and seasonal cycles. Water Resour. Res. 50 (8), 6747–6766.

Holman, R.A., Sallenger Jr, A.H., 1985. Setup and swash on a natural beach. J. Geophys. Res. Oceans 90 (C1), 945–953.

Housego, R., 2021. Barrier Island Groundwater Dynamics. Massachusetts Institute of Technology. Doctoral dissertation.

Housego, R., Raubenheimer, B., Elgar, S., Cross, S., Legner, C., Ryan, D., 2021. Coastal flooding generated by ocean wave-and surge-driven groundwater fluctuations on a sandy barrier island. J. Hydrol. 603, 126920.

Hunt, R.J., Feinstein, D.T., 2012. MODFLOW-NWT: Robust handling of dry cells using a Newton formulation of MODFLOW-2005. Groundwater 50 (5), 659–663.

Jacob, C.E., 1950. Flow of groundwater. Engineering Hydraulics 321–386.

Jha, M.K., Namgial, D., Kamii, Y., Peiffer, S., 2008. Hydraulic parameters of coastal aquifer systems by direct methods and an extended tide–aquifer interaction technique. Water Resour. Manag. 22 (12), 1899–1923.

Jiao, J.J., Tang, Z., 1999. An analytical solution of groundwater response to tidal fluctuation in a leaky confined aquifer. Water Resour. Res. 35 (3), 747–751. https://doi.org/10.1029/1998WR900075.

Kong, J., Shen, C.-J., Xin, P., Song, Z., Li, L., Barry, D.A., Jeng, D.-S., Stagnitti, F., Lockington, D.A., Parlange, J.-Y., 2013. Capillary effect on water table fluctuations in unconfined aquifers. Water Resour. Res. 49 (5), 3064–3069.

Lautier, J. C. (2009), *Hydrogeologic framework and groundwater conditions in the North Carolina East Central Coastal Plain.* North Carolina Department of Environment and Natural Resources, Division of Water Resources, 2009.

Lazarus, E.D., Murray, A.B., 2011. An integrated hypothesis for regional patterns of shoreline change along the Northern North Carolina Outer Banks, USA. Mar. Geol. 281 (1–4), 85–90.

Lentz, S., Raubenheimer, B., 1999. Field observations of wave setup. J. Geophys. Res. Oceans 104 (C11), 25867–25875.

Levanon, E., Yechieli, Y., Shalev, E., Friedman, V., Gvirtzman, H., 2013. Reliable Monitoring of the Transition Zone Between Fresh and Saline Waters in Coastal Aquifers. Groundwater Monit R 33 (3), 101–110.

Li, L., Barry, D.A., Parlange, J.Y., Pattiaratchi, C.B., 1997. Beach water table fluctuations due to wave run-up: Capillarity effects. Water Resour. Res. 33 (5), 935–945. https://doi.org/10.1029/96WR03946.

Li, L., Barry, D.A., Stagnitti, F., Parlange, J.Y., 2000. Groundwater waves in a coastal aquifer: A new governing equation including vertical effects and capillarity. Water Resour. Res. 36 (2), 411–420. https://doi.org/10.1029/1999WR900307.

Li., L., Cartwright, N., Nielsen, P., & Lockington, D. (2004), Response of coastal groundwater table to offshore storms. *China Ocean Engineering, 18*(3), 423–431.

Longuet-Higgins, M.S., Stewart, R.w., 1964. Radiation stresses in water waves; a physical discussion, with applications. Deep-Sea Res. 11 (4), 529–562.

Mallinson, D.J., Smith, C.W., Culver, S.J., Riggs, S.R., Ames, D., 2010. Geological characteristics and spatial distribution of paleo-inlet channels beneath the outer banks barrier islands, North Carolina, USA. Estuar. Coast. Shelf Sci. 88 (2), 175–189.

Manahan, S., Martin, W.K., Guo, W., 1998. Dare County-wide hydrogeological study and groundwater resource evaluation. Dare County Water Production Department, Kill Devil Hills, NC.

Meisburger, E. P., Williams, S. J., & Judge, C. (1989), *Physiographic and geological setting of the Coastal Engineering Research Center's Field Research Facility.* Vicksburg, MS.

Moore, W.S., 2010. The effect of submarine groundwater discharge on the ocean. Ann. Rev. Mar. Sci. 2 (1), 59–88. https://doi.org/10.1146/annurev-marine-120308-081019.

Mulligan, A.E., Langevin, C., Post, V.E.A., 2011. Tidal boundary conditions in SEAWAT. Groundwater 49 (6), 866–879. https://doi.org/10.1111/j.1745-6584.2010.00788.x.

Naba, B., Boufadel, M.C., Weaver, J., 2002. The role of capillary forces in steady-state and transient seepage flows. Groundwater 40 (4), 407–415.

Nielsen, P., 1988. Wave setup: A field study. J. Geophys. Res. 93 (C12), 15643. https://doi.org/10.1029/JC093iC12p15643.

Nielsen, P., 1990. Tidal dynamics of the water table in beaches. Water Resour. Res. 26 (9), 2127–2134. https://doi.org/10.1029/WR026i009p02127.

Nielsen, P., Perrochet, P., 2000a. Watertable dynamics under capillary fringes: experiments and modelling. Adv. Water Resour. 23 (5), 503–515.

Nielsen, P., Perrochet, P., 2000b. ERRATA: Watertable dynamics under capillary fringes: experiments and modeling [Advances in Water Resources 23 (2000) 503–515]. Adv. Water Resour. 23 (8), 907–908.

Nielsen, P., Turner, I., 2000. Groundwater waves and water exchange in beaches. In *27th International Conference on Coastal Engineering.* American Society of Civil Engineers, Sydney, NSW, Australia.

Nielsen, P., Aseervatham, R., Fenton, J.D., Perrochet, P., 1997. Groundwater waves in aquifers of intermediate depths. Adv. Water Resour. 20 (1), 37–43. https://doi.org/10.1016/S0309-1708(96)00015-2.

Niswonger, R. G., Panday, S., & Motomu, I. (2011), *MODFLOW-NWT, A Newton formulation for MODFLOW-2005: U.S. Geological Survey Techniques and Methods 6–A37.*

Parlange, J.-Y., Stagnitti, F., Starr, J.L., Braddock, R.D., 1984. Free-surface flow in porous media and periodic solution of the shallow-flow approximation. J. Hydrol. 70 (1-4), 251–263.

Rakhimbekova, S., Wu, M.Z., Post, V., Robinson, C.E., 2022. Effect of time-varying wave conditions on the fate of nitrogen in a freshwater unconfined nearshore aquifer. Adv. Water Resour. 167, 104273.

Raubenheimer, B., Guza, R.T., Elgar, S., 1999. Tidal water table fluctuations in a sandy ocean beach. Water Resour. Res. 35 (8), 2313–2320. https://doi.org/10.1029/1999WR900105.

Raubenheimer, B., Guza, R.T., Elgar, S., 2001. Field observations of wave-driven setdown and setup. J. Geophys. Res. Oceans 106 (C3), 4629–4638. https://doi.org/10.1029/2000JC000572.

Riggs, S.R., Cleary, W.J., Snyder, S.W., 1995. Influence of inherited geologic framework on barrier shoreface morphology and dynamics. Mar. Geol. 126 (1–4), 213–234. https://doi.org/10.1016/0025-3227(95)00079-E.

Robinson, M.A., Gallagher, D.L., 1999. A model of ground water discharge from an unconfined coastal aquifer. Groundwater 37 (1), 80–87.

Robinson, C., Gibbes, B., Li, L., 2006. Driving mechanisms for groundwater flow and salt transport in a subterranean estuary. Geophys. Res. Lett. 33 (3), L03402. https://doi.org/10.1029/2005GL025247.

Robinson, C., Li, L., Prommer, H., 2007. Tide-induced recirculation across the aquifer-ocean interface. Water Resour. Res. 43 (7) https://doi.org/10.1029/2006WR005679.

Robinson, C., Xin, P., Li, L., Barry, D.A., 2014. Groundwater flow and salt transport in a subterranean estuary driven by intensified wave conditions. Water Resour. Res. 50 (1), 165–181. https://doi.org/10.1002/2013WR01381.

Röper, T., Kröger, K.F., Meyer, H., Sültenfuss, J., Greskowiak, J., Massmann, G., 2012. Groundwater ages, recharge conditions and hydrochemical evolution of a barrier island freshwater lens (Spiekeroog, Northern Germany). J. Hydrol. 454, 173–186.

Rotzoll, K., El-Kadi, A.I., 2008. Estimating hydraulic properties of coastal aquifers using wave setup. J. Hydrol. 353 (1), 201–213. https://doi.org/10.1016/j.jhydrol.2008.02.005.

Rotzoll, K., Fletcher, C.H., 2013. Assessment of groundwater inundation as a consequence of sea-level rise. Nat. Clim. Chang. 3 (5), 477–481. https://doi.org/10.1038/nclimate1725.

Schultz, G., Ruppel, C., 2002. Constraints on hydraulic parameters and implications for groundwater flux across the upland–estuary interface. J. Hydrol. 260 (1–4), 255–269.

Shih, D.C.F., 2018. Storage in confined aquifer: Spectral analysis of groundwater in responses to Earth tides and barometric effect. Hydrol. Process. 32 (12), 1927–1935.

Shoushtari, S.M.H.J., Cartwright, N., Perrochet, P., Nielsen, P., 2015. Influence of hysteresis on groundwater wave dynamics in an unconfined aquifer with a sloping boundary. J. Hydrol. 531, 1114–1121. https://doi.org/10.1016/J.JHYDROL.2015.11.020.

Shoushtari, S.M.H.J., Cartwright, N., Nielsen, P., Perrochet, P., 2016. The effects of oscillation period on groundwater wave dispersion in a sandy unconfined aquifer: Sand flume experiments and modelling. J. Hydrol. 533, 412–420. https://doi.org/10.1016/J.JHYDROL.2015.12.032.

Smith, A. J., & Hick, W. P. (2001), *Hydrogeology and aquifer tidal propagation in Cockburn Sound, Western Australia*.

Sous, D., Lambert, A., Rey, V., Michallet, H., 2013. Swash-groundwater dynamics in a sandy beach laboratory experiment. Coast. Eng. 80, 122–136. https://doi.org/10.1016/j.coastaleng.2013.05.006.

Stockdon, H.F., Holman, R.A., Howd, P.A., Sallenger Jr, A.H., 2006. Empirical parameterization of setup, swash, and runup. Coast. Eng. 53 (7), 573–588.

Threndyle, R.E., Jamieson, R.C., Kennedy, G., Lake, C.B., Kurylyk, B.L., 2022. Future inundation of coastal on-site wastewater treatment systems in a region with pronounced sea-level rise. J. Hydrol. 614, 128548.

Trefry, M.G., Bekele, E., 2004. Structural characterization of an island aquifer via tidal methods. Water Resour. Res. 40 (1) https://doi.org/10.1029/2003WR002003.

Trefry, M.G., Johnston, C.D., 1998. Pumping test analysis for a tidally forced aquifer. Groundwater 36 (3), 427–433. https://doi.org/10.1111/j.1745-6584.1998.tb02813.x.

Trglavcnik, V., Morrow, D., Weber, K.P., Li, L., Robinson, C.E., 2018. Analysis of tide and offshore storm-induced water table fluctuations for structural characterization of a coastal island aquifer. Water Resour. Res. 54 (4), 2749–2767. https://doi.org/10.1002/2017WR020975.

Turner, I.L., Masselink, G., 1998. Swash infiltration-exfiltration and sediment transport. J. Geophys. Res. Oceans 103 (C13), 30813–30824. https://doi.org/10.1029/98JC02606.

Uchiyama, Y., Nadaoka, K., Rölke, P., Adachi, K., Yagi, H., 2000. Submarine groundwater discharge into the sea and associated nutrient transport in a sandy beach. Water Resour. Res. 36 (6), 1467–1479.

Vitousek, S., Barnard, P.L., Fletcher, C.H., Frazer, N., Erikson, L., Storlazzi, C.D., 2017. Doubling of coastal flooding frequency within decades due to sea-level rise. Sci. Rep. 7, 1–9. https://doi.org/10.1038/s41598-017-01362-7.

Werner, A.D., Lockington, D.A., 2003. Influence of hysteresis on tidal capillary fringe dynamics in a well-sorted sand. Adv. Water Resour. 26 (11), 1199–1204. https://doi.org/10.1016/S0309-1708(03)00107-6.

Winner, M. D. J., & Coble, R. (1996). *Hydrogeologic framework of the North Carolina Coastal Plain*.

Woodruff, J., Irish, J., Camargo, S.J., 2013. Coastal flooding by tropical cyclones and sealevel rise. Nature 504, 44–52. https://doi.org/10.1038/nature12855.

Xin, P., Robinson, C., Li, L., Barry, D.A., Bakhtyar, R., 2010. Effects of wave forcing on a subterranean estuary. Water Resour. Res. 46 (12) https://doi.org/10.1029/2010WR009632.

Yu, S., Wang, C., Li, H., Zhang, X., Wang, X., Qu, W., 2022a. Field and numerical investigations of wave effects on groundwater flow and salt transport in a sandy beach. Water Resour. Res. 58 (11) e2022WR032077.

Yu, S., Zhang, X., Li, H., Wang, X., Wang, C., Kuang, X., 2022b. Analytical study for wave-induced submarine groundwater discharge in subtidal zone. J. Hydrol. 612, 128219.